Bulgarian Chemical Communications, Volume 58, Issue 2 (pp. 162-172) 2026 *DOI: 10.34049/bcc.58.2.5741*

Computational modelling of limonoids from *Melia azedarach* as potential inhibitors of leukemia

H. D. Nguyen*

Faculty of Biology, Thai Nguyen University of Education, Thai Nguyen, 24124, Vietnam

Received: December 24, 2025; Revised: March 03, 2026

Leukemia is a systemic hematological malignancy, characterized by dysregulated survival signaling, in which suppression of apoptosis contributes to disease persistence and treatment resistance. In this study, limonoids from *Melia azedarach* were assessed as potential anti-leukemia agents using multi-computational strategies focused on the anti-apoptotic protein Bcl-xL (PDB: 3SPF), with Venetoclax used as a reference ligand for comparative modeling. Docking of eight candidates identified CPD4 as the top binder (-10.35 kcal/mol), surpassing Venetoclax (-9.87 kcal/mol), and revealed a key hydrogen bond with Arg139, alongside extensive hydrophobic/van der Waals contacts in the conserved pocket. Molecular dynamics simulations spanning 100 ns revealed stable complexes, with CPD4 exhibiting a higher backbone RMSD range than Venetoclax while maintaining comparable compactness. MMGBSA analysis yielded favorable binding for both ligands, giving ΔTOTAL values of -19.73 ± 5.33 kcal/mol for CPD4 and -24.48 ± 9.15 kcal/mol for Venetoclax; CPD4 was driven by strong gas-phase interactions (ΔGGAS -43.86 ± 10.49) but incurred a solvation penalty (ΔGSOLV 24.13 ± 6.62). DFT descriptors showed CPD4 with EHOMO -4.3598 eV, ΔE 3.0037 eV, and ω 2.7193 eV, compared with Venetoclax (-9.0405 eV, 4.8522 eV, and 9.0166 eV). Overall, CPD4 emerges as a promising scaffold for targeting Bcl-xL and warrants further optimization and experimental validation in leukemia research.

Keywords: Anti-apoptosis; Bcl-xL; DFT; Leukemia inhibitor; Limonoids; *Melia azedarach*.

INTRODUCTION

Leukemia is a hematological malignancy driven by genetic and epigenetic disruptions in hematopoietic progenitors, most often arising in the bone marrow and resulting in the excessive proliferation of abnormal leukocytes [1]. Unlike many solid tumors that typically form a localized mass before disseminating, leukemic cells are frequently systemic from early stages, which contributes to aggressive clinical behavior and complicates timely diagnosis and durable disease control [2]. Clinically, leukemia is broadly categorized into acute and chronic entities; within the chronic group, chronic myeloid leukemia accounts for approximately 15% of adult cases [3]. Although chemotherapy remains an important therapeutic option, particularly in advanced disease or when targeted regimens are unsuitable, its utility is often constrained by substantial adverse effects such as infection susceptibility, fatigue, and gastrointestinal toxicity. Together with the emergence of treatment resistance, these limitations motivate the search for alternative agents and complementary strategies that can improve efficacy while reducing toxicity burden [4, 5].

A central biological feature supporting malignant persistence is impaired apoptosis, the genetically unnecessary cells to maintain tissue homeostasis [6], programmed mechanism that removes damaged or unnecessary cells to maintain tissue homeostasis [6]. Cancer cells frequently attenuate apoptotic signaling, enabling survival under oncogenic stress and therapeutic pressure, and thereby facilitating uncontrolled expansion. In this context, Bcl-xL (B-cell lymphoma-extra large) is a key anti-apoptotic regulator that suppresses the intrinsic mitochondrial death pathway by limiting cytochrome c release and downstream caspase activation [7, 8]. Its frequent overexpression across cancers has made Bcl-xL an established target for anticancer drug discovery.

Natural products remain a rich source of bioactive scaffolds, and limonoids. Highly oxygenated triterpenoids, abundant in citrus and *Meliaceae* plants, are of particular interest due to reported anticancer, anti-inflammatory, and antiviral activities [9, 10]. Prior studies have identified limonoids from *Melia azedarach*, including pungiolide-type structures, with notable cytotoxicity against multiple human cancer cell lines, including the HL-60 leukemia model [11]. However, the molecular basis of these effects, especially at the level of target-specific recognition and stability, has not been comprehensively examined using modern computational pipelines. Accordingly, this study investigates limonoids from *M. azedarach* as prospective anti-leukemia agents by applying structure-based modelling to characterize their interactions with relevant protein targets, prioritize promising binders within a defined binding region,

---

* To whom all correspondence should be sent: Email*:* *hungnd@tnue.edu.vn*

and estimate developability-related properties, thereby providing a rationale for subsequent experimental validation *in vitro* and *in vivo*.

MATERIALS AND METHODS

Structural preparation of selected limonoids

The selected limonoids from *M. azedarach* possess significant cytotoxic activity against the HL-60 leukemia cancer cell line [11], including meliarachin C (CPD1), toosendanin (CPD2), 1-*O*-cinnamoyltrichilinin (CPD3), 23-methoxyohchininolide A (CPD4), 3-*O*-deacetyl-4'-demethyl-28-oxosalannin (CPD5), 1-*O*-detigloyl-1-*O*-benzoylohchinolal (CPD6), nimbolinin D (CPD7), meliasenin E (CPD8), which have molecular formulas of $C_{31}H_{40}O_{11}$, $C_{30}H_{38}O_{11}$, $C_{39}H_{46}O_9$, $C_{37}H_{44}O_{10}$, $C_{31}H_{38}O_9$, $C_{36}H_{42}O_{10}$, $C_{36}H_{44}O_9$, $C_{31}H_{48}O_5$, respectively, with molecular weights of 588.2571, 574.2414, 658.3142, 648.2934, 554.2516, 634.2778, 620.2985, and 500.3502 g/mol. Venetoclax, possessing a molecular formula of $C_{45}H_{50}ClN_7O_7S$ and a molecular weight of 867.3181 g/mol, was included as a reference Bcl-xL ligand for comparative docking and simulation analyses (Fig. 1).

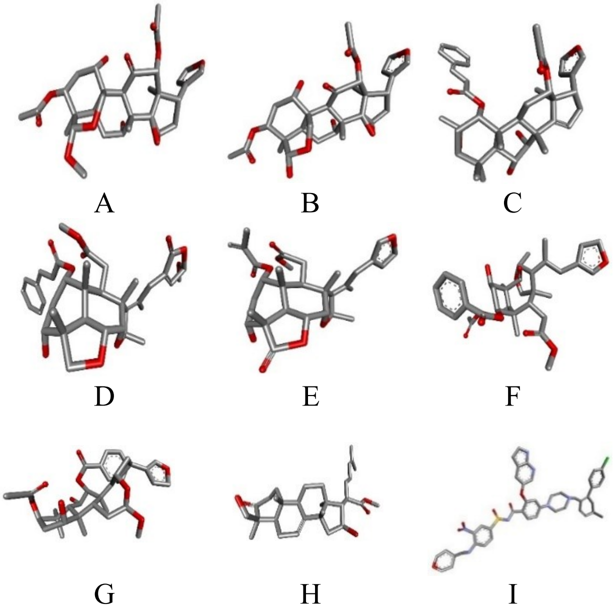

Figure 1. 3D Structures of selected limonoids (A. CPD1; B. CPD2; C. CPD3; D. CPD4; E. CPD5; F. CPD6; G. CPD7; H. CPD8) and the comparative reference Venetoclax (I).

Molecular docking analysis

The three-dimensional structures of the selected limonoids were generated in PDB format using the Biovia Discovery Studio Visualizer 2024 (Dassault Systèmes, San Diego, CA, USA). This process involved adding polar hydrogens, calculating Gasteiger charges, and considering torsional bond flexibility. The structure of the Bcl-xL protein (PDB ID: 3SPF) was retrieved in PDB format from the RCSB Protein Data Bank [12]. Ligand-protein docking simulations were performed using AutoDock Tools, with a grid box spanning 60 points in each x, y, and z dimension at a spacing of 0.375 Å [13]. The binding site coordinates for the Bcl-xL protein were set at x = 32.003 Å, y = 16.833 Å, and z = -18.895 Å. The Lamarckian genetic algorithm was employed to identify low-energy conformations, optimizing the stability of ligand-protein interactions. Following docking, the highest-affinity conformation was evaluated using Biovia Discovery Studio Visualizer 2024 and compared with the docking results obtained for Venetoclax on the same protein to assess similarities in binding interactions.

Molecular dynamics simulation

Molecular dynamics simulations were conducted to examine the highest-affinity docked conformation of the Bcl-xL protein complex (PDB ID: 3SPF) over a period of 100 ns, utilizing GROMACS version 2024.4 [14]. The protein structure was optimized by adding missing atoms and residues, which was accomplished using Swiss-PdbViewer [15]. Ligand force-field parameters were generated through the use of SwissParam [16]. The protein-ligand complex was solvated within a triclinic simulation box using the SPC water model, with 0.15 M NaCl added to maintain an ionic strength of 0.15 M. To ensure structural refinement and charge neutralization, an energy minimization procedure consisting of 50,000 steps was performed. The equilibration process involved a 200 ps NVT ensemble, followed by a 200 ps NPT ensemble, both maintained at 300 K and 1 bar. Three independent production simulations were carried out, each lasting 100 ns with a 2 fs integration step, and the coordinate trajectories were recorded every 10 ns. Analysis of the simulation trajectories was carried out using Grace software, from which key dynamical parameters, including root mean square deviation (RMSD), root mean square fluctuation (RMSF), radius of gyration (Rg), number of hydrogen bonds (Hbonds), and solvent-accessible surface area (SASA), were derived. The stability of the conformations across the simulated complexes was evaluated using UCSF Chimera version 1.13.3 through structural superposition [17].

Molecular mechanics generalised Born surface area (MMGBSA) analysis

Binding free energies for the CPD4-3SPF and Venetoclax-3SPF complexes were computed using the gmx_MMPBSA package, along with the charmm36 force field. The polar solvation energy was determined *via* the generalized Born implicit solvent model, while non-polar contributions were derived from estimations of the solvent-accessible surface area. Data extraction was performed from molecular dynamics trajectories consisting of 125 equally spaced frames, sampled every 80 ps, over an 80 ns duration (ranging from 20 ns to 100 ns). This ensemble-averaging approach allowed for the identification of differences in ligand-protein interaction energetics, thus providing insights into the relative binding affinities and the stability of the complexes during the simulation period [18].

Assay protocol for ADMET prediction

A preliminary assessment of ADMET (Absorption, Distribution, Metabolism, Excretion, Toxicity) properties is essential for predicting pharmacokinetic challenges and safety concerns during the drug discovery process. This approach helps reduce failure rates in later stages and improves the selection of compounds with suitable therapeutic potential. In this study, the pkCSM platform was utilized to predict the ADMET profiles of CPD4 and Venetoclax. This platform employs graph-based molecular descriptors to estimate parameters related to absorption, distribution, metabolism, excretion, and toxicity, facilitating a comprehensive comparison of the key developability features of the compounds under investigation [19].

Quantum chemistry computation using the Density Functional Theory (DFT) method

Molecular geometry optimization for CPD4 and Venetoclax was carried out using the ORCA quantum chemistry package, version 6.1.0 [20]. Initial coordinates were generated in Avogadro [21], and the subsequent visualization of molecular orbitals, along with associated analyses, was performed using IboView version 20211019 [22]. All DFT calculations employed B3LYP/6-31G(d,p) to describe the ground-state electronic structure (electron density and Kohn-Sham orbitals) used to derive frontier-orbital energies and conceptual-DFT descriptors. From the fully optimized molecular structures, key quantum-chemical descriptors were extracted, including the energies of the highest occupied molecular orbital (HOMO) and lowest unoccupied molecular orbital (LUMO), the HOMO-LUMO energy gap (ΔE), chemical potential (μ), electronegativity (χ), global hardness (η), softness (σ), and electrophilicity index (ω). The determination of these reactivity parameters was conducted in accordance with Koopmans' theorem, providing insights into the electronic properties and chemical behavior of the compounds studied [18].

RESULTS AND DISCUSSION

Molecular docking analysis

Molecular docking was employed as an initial structure-based screening approach to estimate the binding propensity of the selected small molecules toward Bcl-xL and to delineate the residue-level determinants underlying ligand recognition. This workflow enables rapid ranking of candidates according to predicted binding free energy surrogates while simultaneously providing interpretable interaction fingerprints, including key pocket-lining residues and hydrogen-bond partners [23]. Accordingly, comparative docking analysis was performed for the selected ligands alongside Venetoclax, a reference Bcl-xL binder, to contextualize candidate binding within a common structural framework before advancing to dynamic stability assessment.

Before ligand docking with protein 3SPF, the binding-pocket residues were defined. Structural inspection of 3SPF in BIOVIA Discovery Studio Visualizer identified key inhibition-associated sites (Fig. 2A). The docking workflow was then validated by redocking the co-crystallized ligand (Fig. 2B), with an RMSD of 1.4637 Å, and the close superimposition with the native pose supported the accuracy of the procedure. An RMSD value below 2 Å is commonly accepted as evidence of a reliable docking protocol [24]. Docked poses were ranked according to the most favorable (lowest) binding energy (kcal/mol).

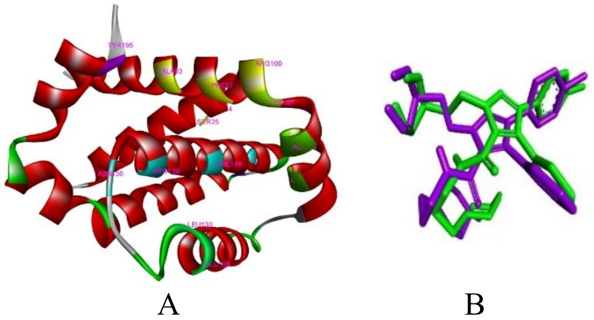

Figure 2. Active sites within the 3SPF protein (A) and superimposition of the docked and native ligands for validation of the molecular docking protocol (violet = native, green = docked) (B).

As summarized in Table 1, docking scores and residue-level contact profiles were evaluated for eight selected ligands within the Bcl-xL binding cavity, with Venetoclax included as a benchmark. Across the candidate set, the interaction field converged on a recurrent pocket architecture dominated by Phe97, Tyr101, Ala104, Phe105, Leu108, Arg139, and Phe146, indicating preferential recognition of a shared binding region. Such complexes are commonly stabilized through a combination of hydrophobic enclosure by aromatic/aliphatic side chains, shape complementarity that optimizes van der Waals contacts, and directional hydrogen bonding that restricts ligand orientation and supports pose persistence within the cavity [25, 26].

Predicted binding energies for CPD1-CPD8 spanned -10.35 to -8.08 kcal/mol, while Venetoclax exhibited a docking score of -9.87 kcal/mol under the same protocol. Within the candidate series, CPD4 produced the most favorable affinity (-10.35 kcal/mol), exceeding the predicted stabilization of Venetoclax. CPD4 occupied the conserved pocket lined by Phe97, Tyr101, Ala104, Phe105, Leu108, Arg139, and Phe146, and additionally involved Asn136, suggesting an expanded polar-contact network relative to several other candidates (Fig. 3A). A hydrogen-bond interaction was annotated with Arg139, consistent with a plausible anchoring role for this residue, while hydrophobic residues (Phe97, Phe105, Leu108, Phe146) provide enclosure. Among the remaining candidates, CPD7 (-9.90 kcal/mol) and CPD5 (-9.78 kcal/mol) approached the reference score. Yet, their contact patterns differed from the most conserved signature: CPD7 engaged a reduced residue subset (Phe97, Ala104, Phe105, Phe146) and formed hydrogen bonds with Val126 and Ser145, whereas CPD5 retained the canonical residue ensemble (Phe97, Tyr101, Ala104, Phe105, Leu108, Arg139, Phe146) with hydrogen bonding to Arg139. By contrast, Venetoclax interacted with a broader region that included Ala93 and Arg100, in addition to the shared core residues. Hydrogen bonding was observed between Arg100 and Gly138, reflecting a distinct anchoring arrangement relative to the selected ligands (Fig. 3B).

Collectively, the docking outcomes indicate that the strongest predicted affinity coincides with the engagement of conserved pocket residues and a defined polar anchor. On this basis, CPD4 was selected for subsequent molecular dynamics simulations, with Venetoclax retained as the comparator to assess the relative stability of the complex, the persistence of key contacts (notably Arg139 for CPD4), and pocket adaptability under explicit-solvent, fully flexible conditions.

Table 1. Interactions between the docked ligands and the protein 3SPF.

Docked ligands	Binding energy (kJ/mol)	Hydrogen bond interaction	Van der Waals interaction	Hydrophobic interaction
CPD1	-8.31	Val126, Arg139	Phe97, Tyr101, Ala104, Val127, Glu129, Asp133, Ala142, Phe146	Phe105, Leu108, Val126, Leu130, Arg139, Ala149
CPD2	-8.08	Val126, Arg139	Phe97, Val127, Glu129, Ala142, Phe146	Tyr101, Ala104, Phe105, Leu108, Val126, Leu130, Ala149
CPD3	-8.44	Arg139	Phe97, Tyr101, Ala104, Leu108, Glu129, Leu130, Gly138	Phe105, Val126, Arg139, Ala142, Phe146
CPD4	-10.35	Arg139	Phe97, Leu108, Val126, Glu129, Leu130, Asp133, Asn136, Ala142, Ser145, Phe146, Ala149	Tyr101, Ala104, Phe105, Arg132
CPD5	-9.78	Arg139	Phe97, Tyr101, Ala104, Asp107, Leu108, Val126, Ser145, Phe146, Ala149	Phe105, Leu130, Arg139, Ala142
CPD6	-8.19	Glu129, Phe146	Phe97, Tyr101, Phe105, Asp107, Leu108, Arg139, Ala142, Ser145, Ala149	Leu130
CPD7	-9.90	Val126, Ser145	Phe97, Phe105, Glu129, Leu130, Ala142, Phe143	Ala104, Phe146, Ala149
CPD8	-8.19	Arg139	Tyr101, Phe105, Leu108, Val126, Glu129, Asp133, Asn136, Phe146	Phe97, Ala104, Leu130, Arg132, Arg139, Ala142
Venetoclax	-9.87	Arg100, Gly138	Glu96, Gln111, Asn136, Ser145, Phe146	Ala193, Phe97, Tyr101, Ala104, Phe105, Leu108, Val126, Leu130, Arg139, Ala142, Tyr195

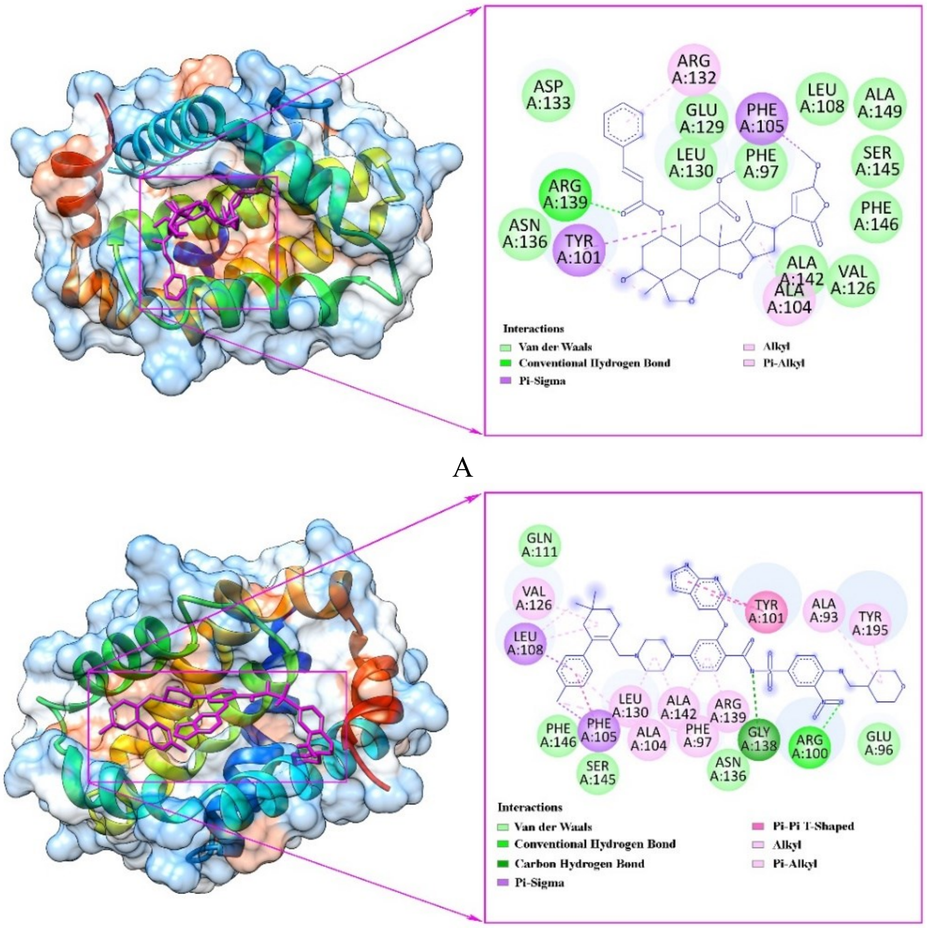

A

B

Figure 3. Molecular docking model and 2D interaction diagram of CPD4 (A) and Venetoclax (B) with 3SPF protein

Notably, the previous study showed that CPD4 exhibited potent cytotoxic activity against HL60 cells with an IC_{50} of 4.9±0.5 μM [11], although it was not the most active compound in the experimental series. Therefore, the present docking results should be interpreted as supporting a putative interaction of CPD4 with the same or an overlapping Bcl-xL binding region used for comparative modeling, rather than as proof that it shares the same experimentally validated mechanism of action as Venetoclax.

Molecular dynamics simulation

To extend the docking observations into a fully flexible, explicitly solvated environment, molecular dynamics simulations were conducted to interrogate the conformational stability and interaction persistence of the two representative predicted bound states. Accordingly, 100-ns trajectories were generated for the CPD4-3SPF and Venetoclax-3SPF complexes, and the resulting ensembles were quantified using RMSD, RMSF, Rg, Hbonds, and SASA to gauge solvent exposure [27]. Consequently, the total energy and potential energy values for the CPD4-3SPF complex were found to be -506,377 kJ/mol and -625,054 kJ/mol, respectively. For the Venetoclax-3SPF complex, the total and potential energy values were -230,784,598 kJ/mol and -287,485 kJ/mol, respectively. The simulation system maintained equilibrium at 300 K.

In Figure 4A, both complexes showed an initial relaxation followed by stable RMSD fluctuations without sustained drift over 100 ns. CPD4-3SPF sampled a higher RMSD range (0.25-0.30 nm, occasionally 0.32 nm), whereas Venetoclax-3SPF remained lower and tighter (0.22-0.25 nm, occasionally 0.26 nm), supporting overall fold stability with slightly reduced global deviation for Venetoclax [28].

RMSF analysis of the Met1-Asn197 segment (Fig. 4B) indicated that the most significant motions were restricted to the extreme N-terminus, peaking at 0.40 nm for CPD4-3SPF and 0.25 nm for Venetoclax-3SPF. Outside this region, fluctuations rapidly decreased and remained low across the rest of the segment (0.04-0.06 nm), with CPD4 showing only slightly higher amplitudes and no evidence of localized destabilization.

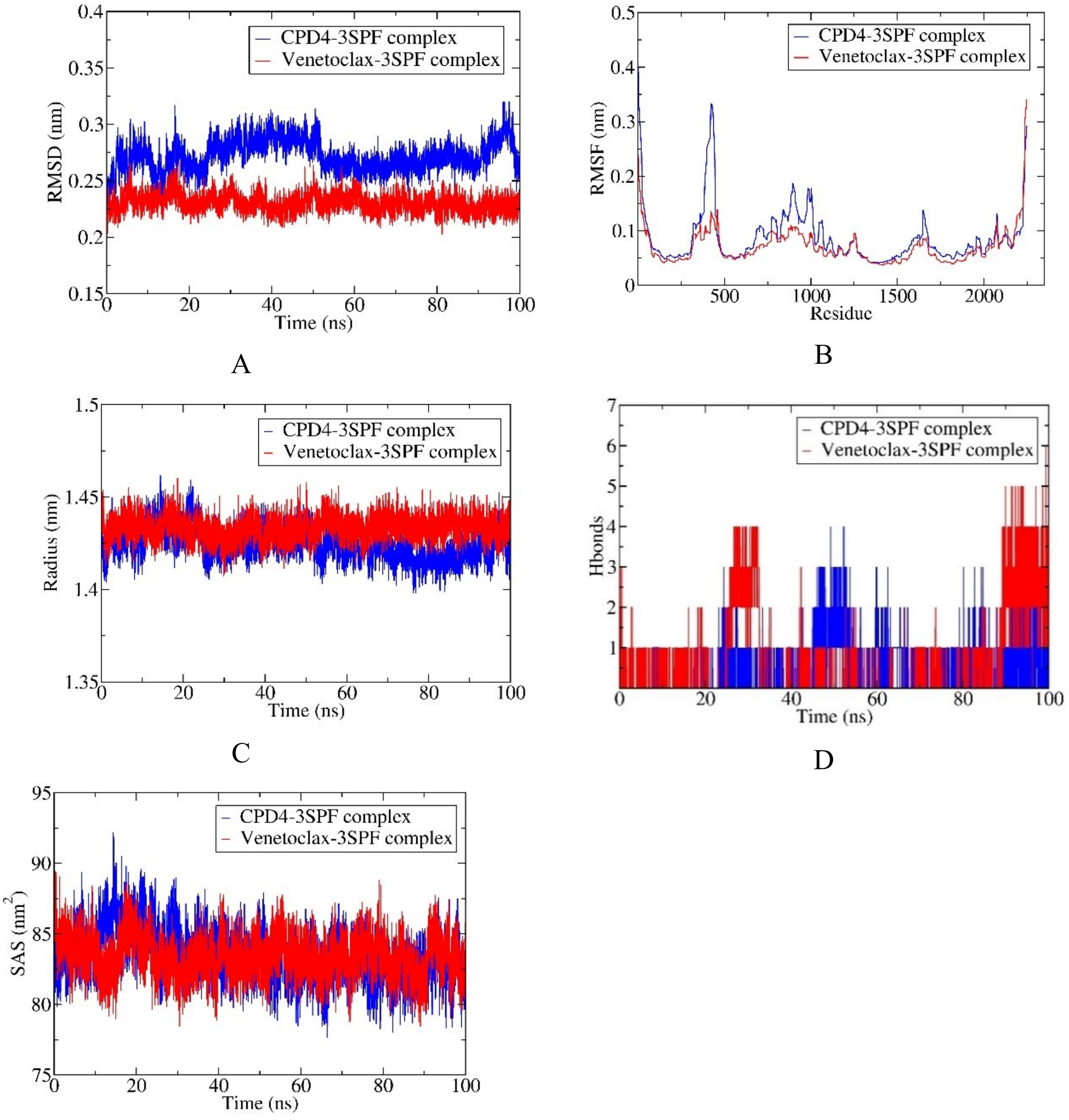

A

B

C

D

E

Figure 4. Results of MD simulation for the bindings of CPD4 (blue) and Venetoclax (red) with 3SPF protein. (A) RMSD, (B) RMSF, (C) Rg, (D) Hbonds, (E) SASA

The radius of gyration (Rg) reports mass-weighted compactness. Over the simulation (Fig. 4C), both complexes remained within a narrow Rg range of 1.41-1.46 nm, indicating a stable global structure; CPD4-3SPF tended to slightly lower values, especially later in the trajectory, while Venetoclax-3SPF more often occupied the upper part of the same band.

The intermolecular number of hydrogen bonds summarizes the persistence of polar contacts at the binding interface. In Figure 4D, both complexes were typically dominated by 0-1 hydrogen bond, but CPD4-3SPF showed a mid-trajectory enrichment (45-60 ns) with repeated sampling of 1-3 and brief peaks at 4, whereas Venetoclax-3SPF exhibited stronger episodes around 25-35 ns (up to 4) and 90-100 ns, where counts frequently reached 3-5 and occasionally 6, indicating more frequent high-occupancy polar anchoring for Venetoclax.

SASA, a proxy for overall solvent exposure, remained stable for both complexes over 100 ns (Fig. 4E), with values ranging from 78 to 90 nm² and no sustained trends. CPD4 showed brief early increases but more often occupied the lower end of the shared band later. In contrast, Venetoclax sampled slightly higher values on average, indicating only modest differences in solvent exposure rather than major structural rearrangements [29].

Collectively, the five readouts support the formation of dynamically stable protein scaffolds for both CPD4-3SPF and Venetoclax-3SPF over 100 ns. The CPD4 complex exhibited a higher RMSD band. It enhanced residue-level flexibility in specific internal regions, accompanied by slightly reduced compactness and marginally lower solvent exposure during the later simulation segments. The Venetoclax complex exhibited lower global deviation and displayed more frequent high-count hydrogen-bond episodes, particularly towards the end of the trajectory, consistent with the episodic strengthening of polar contacts while maintaining overall structural stability.

Free binding energy (MMGBSA) analysis

MMGBSA approximates ligand-protein association by combining molecular mechanics interaction energies with an implicit-solvent model, in which polar solvation is treated using the generalized Born method and nonpolar solvation is estimated from solvent-accessible surface area. It is commonly used for relative ligand ranking under a consistent protocol; however, outcomes depend on parameter choices and sampling, and it omits explicit entropy. Therefore, the results should be interpreted comparatively rather than as absolute free energies. As detailed in Table 2, both CPD4 and Venetoclax yield negative mean ΔTOTAL values, supporting a favorable association in the MMGBSA sense. CPD4-3SPF shows ΔTOTAL = -19.73 ± 5.33 kcal/mol, whereas Venetoclax-3SPF is more negative at -24.48 ± 9.15 kcal/mol, indicating a modestly stronger mean binding estimate for Venetoclax in this dataset. The larger dispersion for Venetoclax suggests a broader distribution of sampled binding microstates, consistent with its more variable energetic terms across the trajectory.

Table 2. Free energy of binding obtained using MMGBSA calculations.

Energy component	Average (kcal/mol)		Standard deviation	
	CPD4-3SPF	Venetoclax-3SPF	CPD4-3SPF	Venetoclax-3SPF
ΔVDWAΔALS	-30.40	-42.38	4.45	8.78
ΔEEL	-13.47	76.27	7.69	28.36
ΔEGB	28.18	-52.84	6.93	26.26
ΔESURF	-4.05	-5.53	0.57	1.25
ΔGGAS	-43.86	33.89	10.49	32.24
ΔGSOLV	24.13	-58.36	6.62	25.52
ΔTOTAL	-19.73	-24.48	5.33	9.15

MMGBSA decomposition suggests that CPD4 binding is primarily driven by favorable gas-phase interactions, with ΔVDWAΔALS = -30.40 ± 4.45 kcal/mol and ΔEEL = -13.47 ± 7.69 kcal/mol, resulting in ΔGGAS = -43.86 ± 10.49 kcal/mol. This gain is partly offset by a net solvation penalty (ΔGSOLV = 24.13 ± 6.62 kcal/mol), dominated by polar desolvation (ΔEGB = 28.18 ± 6.93 kcal/mol), while the nonpolar term remains favorable but smaller (ΔESURF = -4.05 ± 0.57 kcal/mol). Venetoclax shows the opposite balance: despite strong van der Waals stabilization (ΔVDWAΔALS = -42.38 ± 8.78 kcal/mol), its electrostatics are unfavorable on average (ΔEEL = 76.27 ± 28.36 kcal/mol), giving a positive ΔGGAS of 33.89 ± 32.24 kcal/mol that is overcompensated by highly favorable solvation (ΔGSOLV = -58.36 ± 25.52 kcal/mol), mainly driven by ΔEGB = -52.84 ± 26.26 kcal/mol and supported by ΔESURF = -5.53 ± 1.25 kcal/mol. Overall, CPD4 appears more contact-driven but desolvation-limited, whereas Venetoclax achieves a slightly more favorable net ΔTOTAL through solvation compensation and shows greater energetic variability across the trajectory.

Table 3. Predicted ADMET properties of CPD4 and Venetoclax

ADMET properties	Unit	CPD4	Venetoclax
Water solubility	(Log mol/L)	-4.542	-3.037
Caco2 permeability	(Log Papp in 10^{-6} cm/s)	0.876	0.847
Intestinal absorption (human)	(% Absorbed)	97.76	100
Skin permeability	(Log Kp)	-2.755	-2.735
P-glycoprotein substrate	Yes/No	No	Yes
P-glycoprotein I inhibitor	Yes/No	Yes	Yes
P-glycoprotein II inhibitor	Yes/No	Yes	Yes
VDss	(Log L/kg)	-0.469	-0.329
Fraction unbound (human)	(Fu)	0	0.169
BBB permeability	(Log BB)	-1.362	-1.747
CNS permeability	(Log PS)	-2.721	-3.119
CYP2D6 substrate	Yes/No	No	No
CYP3A4 substrate	Yes/No	Yes	Yes
CYP1A2 inhibitor	Yes/No	No	No
CYP2C19 inhibitor	Yes/No	No	No
CYP2C9 inhibitor	Yes/No	No	No
CYP2D6 inhibitor	Yes/No	No	No
CYP3A4 inhibitor	Yes/No	Yes	Yes
Total clearance	(Log ml/min/kg)	0.137	-0.096
Renal OCT2 substrate	Yes/No	No	No
AMES toxicity	Yes/No	No	No
Max. tolerated dose (human)	(Log mg/kg/day)	-0.208	0.278
hERG I inhibitor	Yes/No	No	No
hERG II inhibitor	Yes/No	No	Yes
Oral rat acute toxicity (LD50)	(mol/kg)	2.291	2.604
Oral rat chronic toxicity (LOAEL)	(Log mg/kg_ bw/day)	1.03	1.924
Hepatotoxicity	Yes/No	No	Yes
Skin sensation	Yes/No	No	No
Tetrahymena pyriformis toxicity	(Log µg/L)	0.285	0.285
Minnow toxicity	(Log mM)	0.442	-0.481

ADMET prediction analysis

In silico ADMET profiling was used to compare the predicted pharmacokinetic behavior and safety-relevant flags of CPD4 with those of Venetoclax, with descriptors grouped into absorption, distribution, metabolism, excretion, and toxicity (Table 3). This side-by-side comparison provides an early indication of potential developability trade-offs that may complement the docking and molecular dynamics prioritization.

For absorption, CPD4 shows lower predicted water solubility than Venetoclax (-4.542 *vs* -3.037 log mol/L), indicating a greater dissolution constraint. By contrast, Caco-2 permeability is similar (0.876 *vs* 0.847 log Papp), and both retain very high intestinal absorption (97.76% *vs* 100%) with comparable skin permeability (-2.755 *vs* -2.735 log Kp) [30]. Both ligands exhibit low VDss (-0.469 for CPD4 and -0.329 log L/kg for Venetoclax), but binding differs markedly, with Fu = 0 for CPD4 versus 0.169 for Venetoclax. CPD4 also shows higher predicted BBB/CNS permeability (log BB -1.362 *vs* -1.747; log PS -2.721 *vs* -3.119), although both indicate limited overall penetration [31]. For metabolism, the two compounds share a similar pattern. Neither is predicted to be a CYP2D6 substrate, while both are classified as CYP3A4 substrates. Inhibition liabilities across the screened CYP isoforms are largely absent except for CYP3A4, for which both CPD4 and Venetoclax are predicted inhibitors, suggesting a comparable potential for CYP3A4-related interaction risk in this specific output [32]. CPD4 shows a higher predicted total clearance than Venetoclax (0.137 vs -0.096 log ml/min/kg). Neither compound is predicted to be a renal OCT2 substrate, indicating that it is not designated as an OCT2 substrate in the current panel. For toxicity, both compounds are AMES-negative and are not predicted to inhibit hERG I; however, Venetoclax is flagged as a hERG II inhibitor, while CPD4 is not. CPD4 shows a lower predicted maximum tolerated dose (-0.208 *vs* 0.278 log mg/kg/day) and lower LD50 and LOAEL values (2.291 *vs* 2.604 mol/kg; 1.03 *vs* 1.924 log mg/kg_bw/day), whereas hepatotoxicity is predicted only for Venetoclax; skin sensitization is negative for both, *Tetrahymena pyriformis* toxicity is identical (0.285 log µg/L), and Minnow toxicity differs (0.442 *vs* -0.481 log mM). Overall, CPD4 is predicted to have high absorption with similar Caco-2 permeability but lower solubility and Fu, while lacking P-gp substrate status and the hERG II flag seen for Venetoclax. Venetoclax is more soluble and less protein-bound, but is predicted to be a P-gp substrate with hERG II inhibition and hepatotoxicity alerts, despite a higher tolerated dose and more favorable rodent toxicity indices. The Boiled-egg model was additionally applied (Fig. 5). CPD4 was positioned in the white region but outside the yellow yolk, supporting high GI absorption and low BBB permeation, whereas Venetoclax was out of range and therefore not displayed in the plot.

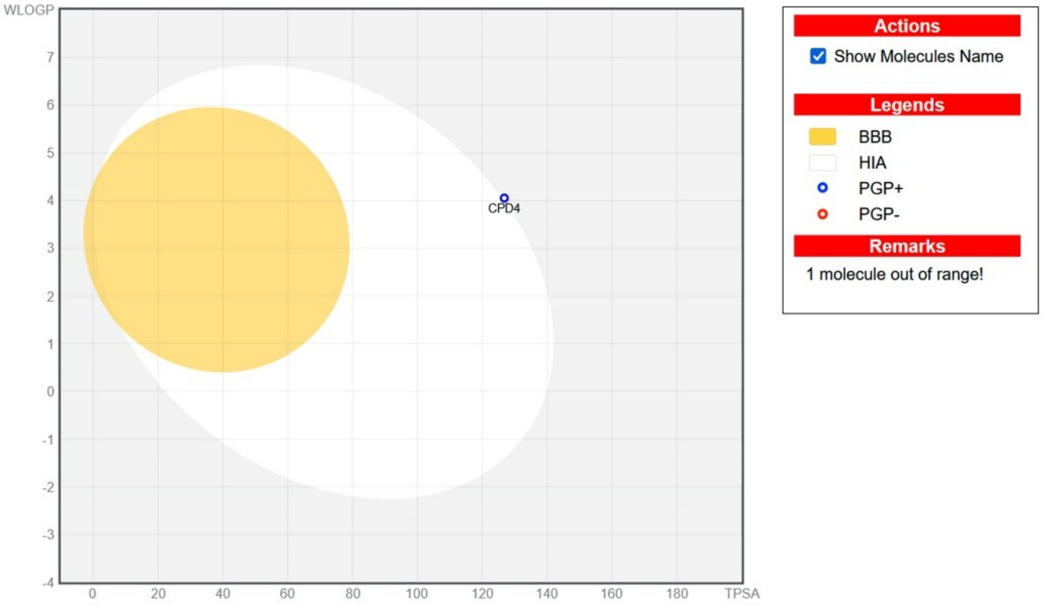

Figure 5. Boiled-egg plot of the selected compounds, generated from Swiss ADME

Table 4. Quantum descriptors of CPD4 and Venetoclax.

Molecule	EHOMO (eV)	ELUMO (eV)	ΔE (eV)	μ (eV)	χ (eV)	η (eV)	σ (eV^{-1})	ω (eV)
CPD4	-4.3598	-1.3561	3.0037	-2.8580	2.8580	1.5019	0.6658	2.7193
Venetoclax	-9.0405	-4.1883	4.8522	-6.6144	6.6144	2.4261	0.4122	9.0166

EHOMO (eV): highest occupied molecular orbitals; ELUMO (eV): lowest unoccupied molecular orbitals; ΔE (eV): energy gap; μ (eV): chemical potential; χ (eV): electronegativity; η (eV): hardness; σ (eV^{-1}): softness; ω (eV): electrophilicity index.

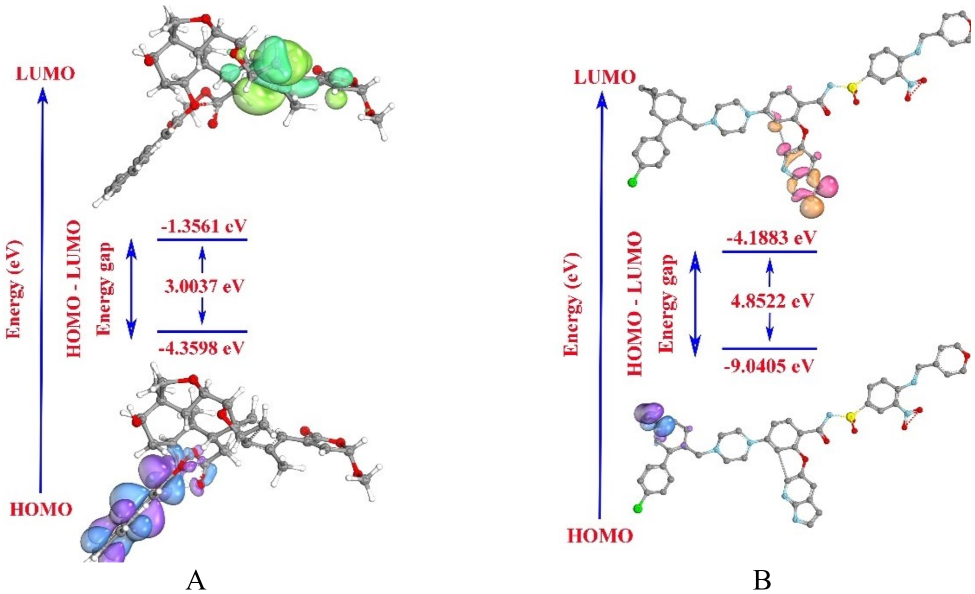

Figure 6. HOMO and LUMO surface diagrams of CPD4 (A) and Venetoclax (B)

Quantum chemistry computation using the DFT method

DFT calculations were performed to complement the docking, molecular dynamics, and MMGBSA analyses by characterizing the electronic structure of CPD4 in comparison with the reference compound Venetoclax. CPD4 exhibits EHOMO (eV) = -4.3598, whereas Venetoclax shows a substantially lower value (-9.0405). Within the usual frontier-orbital interpretation, the less damaging EHOMO for CPD4 is consistent with a comparatively greater propensity to donate electron density relative to Venetoclax under the same theoretical level (Table 4). For the acceptor channel, CPD4 has ELUMO (eV) = -1.3561, while Venetoclax presents -4.1883, indicating that Venetoclax possesses a lower-lying acceptor orbital in this calculation. The combined consequence is a markedly smaller ΔE (eV): energy gap for CPD4 (3.0037) than for Venetoclax (4.8522) (Fig. 6). A reduced gap is commonly associated with increased electronic responsiveness and easier polarization, whereas a larger gap is typically interpreted as greater intrinsic electronic stability.

Frontier-orbital and global conceptual-DFT descriptors provide a qualitative link between electronic structure and noncovalent recognition. A smaller HOMO-LUMO gap (ΔE) generally implies higher electronic polarizability/softness and easier charge redistribution upon environmental perturbation, which can facilitate adaptation to the electrostatic field of the binding pocket and strengthen polarization-driven contributions to binding. In contrast, a larger ΔE is often associated with higher intrinsic electronic stability and lower responsiveness. The electrophilicity index (ω) reflects the tendency to accept electron density; ligands with higher ω typically display a stronger electron-accepting character and may engage more favorably in interactions where electron density donation from the protein stabilizes the complex. These descriptors help rationalize the observed differences in electrostatic and solvation terms in MMGBSA and complement the molecular docking and molecular dynamics simulations results as an electronic-structure perspective rather than a direct quantitative predictor of potency [33], [34].

Global descriptors further distinguish the ligands: Venetoclax has a more negative μ (-6.6144 *vs* -2.8580 eV) and higher χ (6.6144 *vs* 2.8580 eV), indicating stronger electron-attracting character, together with higher η (2.4261 *vs* 1.5019 eV) and lower σ (0.4122 *vs* 0.6658 eV^{-1}), consistent with greater resistance to charge redistribution than CPD4. This separation is reinforced by the electrophilicity index, where ω is significantly higher for Venetoclax (9.0166 eV) than for CPD4 (2.7193 eV), supporting a more electrophilic signature that may relate to the distinct electrostatic-solvation balance observed in the MMGBSA analysis.

CONCLUSION

This study performed computational modelling of limonoids from *M. azedarach* as potential inhibitors of leukemia, focusing on the Bcl-xL protein (3SPF). CPD4 showed the best docking score compared with Venetoclax, forming a hydrogen bond with Arg139 and extensive hydrophobic and van der Waals interactions within the conserved pocket. During 100 ns molecular dynamics, both complexes remained stable; CPD4 sampled a higher RMSD range than Venetoclax while maintaining similar compactness, and hydrogen-bond counts were generally low but more frequently elevated for Venetoclax late in the trajectory. MMGBSA supported favorable binding for both ligands, with ΔTOTAL = -19.73 ± 5.33 kcal/mol for CPD4 and -24.48 ± 9.15 kcal/mol for Venetoclax, where CPD4 was driven by gas-phase interactions (ΔGGAS -43.86 ± 10.49) but penalized by solvation (ΔGSOLV 24.13 ± 6.62). DFT descriptors indicated that CPD4 is more polarizable, showing EHOMO = -4.3598 eV, ΔE = 3.0037 eV, and ω = 2.7193 eV, whereas Venetoclax displayed EHOMO = -9.0405 eV, ΔE = 4.8522 eV, and a higher ω = 9.0166 eV. Overall, the integrated results position CPD4 as a promising computational hit for further optimization and experimental evaluation as a potential Bcl-xL-interacting scaffold in leukemia research. However, the present computational results do not establish that the studied limonoids share the same mechanism of action as Venetoclax, but instead support a possible interaction with the same or an overlapping Bcl-xL pocket region.

REFERENCES

1. S. Ishaq, S. Afzal, S. A. Usmani, I. Wajid, A. Aziz, R. Tahir, A. Ahmad, A. Ullah, *Crit. Rev. Oncol. Hematol.*, **215**, 104909 (2025).
2. S. Shimony, M. Stahl, R. M. Stone, *Am. J. Hematol.*, **98**, 502 (2023).
3. L. Kalinkova, A. Sevcikova, V. Stevurkova, I. Fridrichova, S. Ciernikova, *Int. J. Mol. Sci.*, **24**, 633 (2023).
4. S. Ingole, N. Vasdev, M. Tekade, T. Gupta, B. Pawar, M. Mhatre, A. G. Prasad, R. K. Tekade, Toxic effects of cancer therapies (Public health and toxicology issues in drug research), Academic Press, Boston, 2024.
5. S. K. Jha, N. Singh, O. R. Shanker, I. Antil, J. S. Baghel, V. Huddar, R. Tripathi, *Front. Nat. Prod.*, **4**, 1635197 (2025).
6. J. Plati, O. Bucur, R. Khosravi-Far, *Integr. Biol.*, **3**, 279 (2011).
7. M. Morales-Martínez, M. I. Vega, *Int. J. Mol. Sci.*, **23**, 2193 (2022).
8. P. Ryzhov, Y. Tian, Y. Yao, A. A. Bobkov, W. Im, F. M. Marassi, *Biophys. J.*, **119**, 1324 (2020).
9. Y. S. Shi, Y. Zhang, H. T. Li, C. H. Wu, H. R. El-Seedi, W. K. Ye, Z. W. Wang, C. B. Li, X. F. Zhang, G. Y. Kai, *J. Funct. Foods*, **75**, 104213 (2020).
10. A. Roy, S. Saraf, *Biol. Pharm. Bull.*, **29**, 191 (2006).
11. T. Akihisa, X. Pan, Y. Nakamura, T. Kikuchi, N. Takahashi, M. Matsumoto, E. Ogihara, M. Fukatsu, K. Koike, H. Tokuda, *Phytochemistry*, **89**, 59 (2013).
12. H. Zhou, J. Chen, J. L. Meagher, C. Y. Yang, A. Aguilar, L. Liu, L. Bai, X. Cong, Q. Cai, X. Fang, J. A. Stuckey, S. Wang, *J. Med. Chem.*, **55**, 4664 (2012).
13. G. M. Morris, R. Huey, W. Lindstrom, M. F. Sanner, R. K. Belew, D. S. Goodsell, A. J. Olson, *J. Comput. Chem.*, **30**, 2785 (2009).
14. D. Van Der Spoel, E. Lindahl, B. Hess, G. Groenhof, A. E. Mark, H. J. Berendsen, *J. Comput. Chem.*, **26**, 1701 (2005).
15. N. Guex, M. C. Peitsch, *Electrophoresis*, **18**, 2714 (1997).
16. V. Zoete, M. A. Cuendet, A. Grosdidier, O. Michielin, *J. Comput. Chem.*, **32**, 2359 (2011).
17. E. F. Pettersen, T. D. Goddard, C. C. Huang, G. S. Couch, D. M. Greenblatt, E. C. Meng, T. E. Ferrin, *J. Comput. Chem.*, **25**, 1605 (2004).
18. H. D. Nguyen, *Phys. Chem. Res.*, **13**, 783 (2025).
19. D. E. Pires, T. L. Blundell, D. B. Ascher, *J. Med. Chem.*, **58**, 4066 (2015).
20. F. Neese, *WIREs Comput. Mol. Sci.*, **15**, e70019 (2025).
21. M. D. Hanwell, D. E. Curtis, D. C. Lonie, T. Vandermeersch, E. Zurek, G. R. Hutchison, *J. Cheminform.*, **4**, 17 (2012).
22. G. Knizia, *J. Chem. Theory Comput.*, **9**, 4834 (2013).
23. S. Singh, Q. Bani Baker, D. B. Singh, Molecular docking and molecular dynamics simulation (Bioinformatics), Academic Press, Boston, 2022.
24. D. Ramírez, J. Caballero, *Molecules*, **23**, 1038 (2018).
25. G. Bitencourt-Ferreira, M. Veit-Acosta, W. F. de Azevedo, Hydrogen bonds in protein-ligand complexes (Docking screens for drug discovery), Springer, New York, 2019.
26. G. Bitencourt-Ferreira, M. Veit-Acosta, W. F. de Azevedo, Van der Waals potential in protein complexes (Docking screens for drug discovery), Springer, New York, 2019.
27. Z. Jin, Z. Wei, *Compr. Rev. Food Sci. Food Saf.*, **23**, e13280 (2024).
28. H. Rajput, G. Choudhary, H. Siddiqui, A. Ghosh, M. Prajapat, A. Prakash, B. Medhi, *Indian J. Pharmacol.*, **57**, 308 (2025).
29. H. O. Tekin, G. ALMisned, S. A. M. Issa, E. S. Kasikci, M. Arooj, A. Ene, M. S. Al-Buriahi, M. Konuk, H. M. H. Zakaly, *Front. Phys.*, **10**, 838725

(2022).

30. A. K. Madan, H. Dureja, Prediction of pharmacokinetic parameters (Computational toxicology), Humana Press, Totowa, 2012.
31. P. Sucharitha, K. Ramesh Reddy, S. V Satyanarayana, T. Garg, Absorption, distribution, metabolism, excretion, and toxicity assessment of drugs using computational tools (Computational approaches for novel therapeutic and diagnostic designing to mitigate SARS-CoV-2 infection), Academic Press, Boston, 2022.
32. F. P. Guengerich, *Toxicol. Res.*, **37**, 1 (2021).
33. F. Basha, F. L. A. Khan, S. Muthu, M. Raja, *Comput. Theor. Chem.*, **1198**, 113169 (2021).
34. Y. Huang, C. Rong, R. Zhang, S. Liu, *J. Mol. Model.*, **23**, 3 (2016).